

## Article

# Two Polarity-Sensitive Fluorescent Probes Based on Curcumin Analogs for Visualizing Polarity Changes in Lipid Droplets

Lin Shan <sup>1,2</sup>, Xuewei Li <sup>1,2</sup>, Xiuli Zheng <sup>1</sup>, Jiasheng Wu <sup>1,3</sup>, Haohui Ren <sup>1,3</sup>, Weimin Liu <sup>1,2,\*</sup>  and Pengfei Wang <sup>1,2</sup>

<sup>1</sup> Key Laboratory of Photochemical Conversion and Optoelectronic Materials and CityU-CAS Joint Laboratory of Functional Materials and Devices, Technical Institute of Physics and Chemistry, Chinese Academy of Sciences, Beijing 100190, China

<sup>2</sup> School of Future Technology, University of Chinese Academy of Sciences, Beijing 100049, China

<sup>3</sup> Institute of Optical Physics and Engineering Technology, Qilu Zhongke, Jinan 250000, China

\* Correspondence: wmliu@mail.ipc.ac.cn

**Abstract:** As a class of highly dynamic organelles, lipid droplets (LDs) are involved in numerous physiological functions, and the changes in polarity of LDs are closely related to a variety of diseases. In this work, we developed two polarity-sensitive fluorescent probes (CC-CH and CC-Cl) based on curcumin analogs. CC-CH and CC-Cl with a donor–acceptor–donor (D–A–D) structure exhibited the property of intramolecular charge transfer (ICT); thus, their fluorescence emissions were significantly attenuated with increasing ambient polarity. Cell experiments indicated that CC-CH and CC-Cl showed excellent photostability, a low cytotoxicity, and a superior targeting ability regarding LDs. After treatment with oleic acid (OA) and methyl- $\beta$ -cyclodextrin (M- $\beta$ -CD), the polarity changes of LDs in living cells could be visualized by using CC-CH and CC-Cl. In addition, CC-CH and CC-Cl could monitor polarity changes of LDs in different pathological processes, including inflammatory responses, nutrient deprivation, and H<sub>2</sub>O<sub>2</sub>-induced oxidative stress. Therefore, CC-CH and CC-Cl are promising potential fluorescent probes for tracking intracellular LD polarity changes.

**Keywords:** polarity-sensitive; lipid droplet targeted; fluorescent probes; cell imaging



**Citation:** Shan, L.; Li, X.; Zheng, X.; Wu, J.; Ren, H.; Liu, W.; Wang, P. Two Polarity-Sensitive Fluorescent Probes Based on Curcumin Analogs for Visualizing Polarity Changes in Lipid Droplets. *Molecules* **2023**, *28*, 6626. <https://doi.org/10.3390/molecules28186626>

Academic Editors: Xuewen He and Li-Ya Niu

Received: 28 August 2023

Revised: 11 September 2023

Accepted: 12 September 2023

Published: 14 September 2023



**Copyright:** © 2023 by the authors. Licensee MDPI, Basel, Switzerland. This article is an open access article distributed under the terms and conditions of the Creative Commons Attribution (CC BY) license (<https://creativecommons.org/licenses/by/4.0/>).

## 1. Introduction

Lipid droplets (LDs, also known as lipid bodies or oil bodies) play an indispensable role in the maintenance of cellular energy homeostasis as the center of intracellular lipid storage, metabolism, and transport [1–3]. LDs have neutral lipids [4,5] (the most common components in eukaryotes are triacylglycerols and sterol esters) as the center, surrounded by a phospholipid monolayer modified with a variety of associated proteins [6,7]. They are not an inert organelle, as recognized by humans in earlier times, but are highly dynamic and tightly connected to various organelles [8–10]. LDs are involved in numerous physiological functions including signaling [11,12], buffering of lipotoxicity [13,14], relief of cellular stress [15–17], and modulation of inflammatory responses [18,19]. Dysregulation of LDs is associated with diseases such as obesity [20,21], cardiovascular diseases [22,23], non-alcoholic fatty liver disease (NAFLD) [24–26], diabetes [27–29], neurodegeneration [30,31], and multiple cancers [32,33]. Dysregulation of LDs is usually accompanied by changes in the internal environment of the LDs. Polarity, on the other hand, as an important parameter in the internal environment of LDs, has been proven to be associated with a variety of disease processes [34,35]. Consequently, the development of tools to visualize changes in the polarity of LDs is of great importance for the early diagnosis of diseases and the exploration of disease processes.

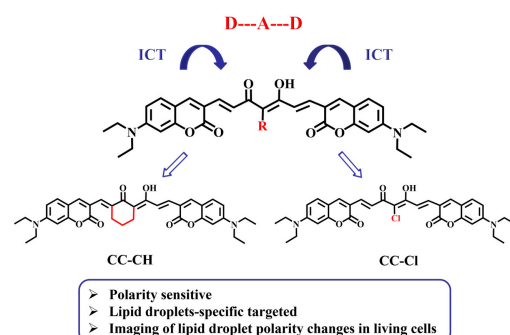
Due to the advantages of a high spatial resolution, high sensitivity, non-invasive nature, simple operation, and low cost, fluorescence imaging technology has a wide range of applications in life sciences, medical diagnosis, and drug development [36,37]. In recent years, with increasing awareness of the importance of LDs, LD-targeted fluorescent probes

based on various fluorescent parent nuclei have been developed [38–40]. However, there are still relatively few probes capable of imaging changes in the polarity of LDs [41], and the photostability of most of them needs to be further improved. Furthermore, the majority of polarity-sensitive LD probes have not yet delved into the relationship between LD polarity and associated pathological processes.

The intramolecular charge transfer (ICT) mechanism [42] has been widely adopted in the construction of LD-targeted polarity-sensitive probes due to the advantages of easy realization and easy adjustment. Polarity-sensitive probes based on the ICT mechanism are usually realized by constructing a  $\pi$ -bonded D–A system [43], where D and A represent an electron donor and an electron acceptor, respectively. In low polarity solvents, the excited state of the probe is presented in the locally excited (LE) state, leading to strong fluorescence emission at short wavelengths, whereas in high polarity solvents, due to strong dipole–dipole interactions between the solvent and the probe, the excited state of the probe exists in a lower energy ICT state, leading to weak fluorescence emission at long wavelengths.

In recent years, a few fluorescent probes based on the D–A structure have been developed for the polarity detection of intracellular LDs [44–47]. For instance, Lin et al. [44] reported a D–A molecule with ICT properties, CTPA, which was sensitive to polarity and specifically targeted LDs. CTPA could distinguish between cancer cells and normal cells based on the difference in polarity. Klymchenko et al. [45] developed a fluorescent probe with the D–A structure: Dimethyl Aniline Furaldehyde (DAF). Under a single excitation source (405 nm laser), DAF enabled the detection of polarity differences within LDs of the same cell, revealing polarity heterogeneity from the core to the edge. Compared with conventional D–A molecules, D–A–D molecules have dual ICT processes due to the fact that the electron acceptor is connected to two electron donors at the same time [48]. They are more favorable for the charge separation of the probe in high polarity solvents as well as the lowering of the excited state energy level, resulting in a higher polarity sensitivity. However, D–A–D molecules for detecting the polarity of LDs have rarely been reported.

In our previous work, we designed an LD-targeted photosensitizer with a D–A–D structure by introducing coumarin into the curcumin skeleton, which exhibited clear photocytotoxicity in a hypoxic microenvironment [49]. In this work, we synthesized two new D–A–D fluorescent probes (CC-CH and CC-Cl) based on curcumin analogs with excellent LD-targeting abilities. In order to increase the stability and extend the emission wavelength, a six membered ring and a chlorine atom were introduced into the coumarin–curcumin framework, respectively (Scheme 1), forming two D–A–D molecules with ICT properties. CC-CH and CC-Cl are polarity sensitive, emit strong fluorescence in low polarity solvents, and significantly attenuate fluorescence in high polarity solvents due to the dipole–dipole interactions in high polarity solvents. Utilizing the superior targeting ability to LDs and good photostability, CC-CH and CC-Cl allow imaging of changes in the size and number of LDs. More significantly, these polarity-sensitive probes can be successfully used for visualization of LD polarity changes in different pathological processes, such as inflammatory responses, nutrient deprivation, and H<sub>2</sub>O<sub>2</sub>-induced oxidative stress.



**Scheme 1.** Structure of CC-CH and CC-Cl.

## 2. Results and Discussion

### 2.1. Photophysical Properties

Initially, we investigated the photophysical properties of CC-CH and CC-Cl in organic solvents with different polarities. As shown in Figure 1a, the absorption spectra of CC-CH showed a positive solvatochromic shift from toluene (498 nm) to DMSO (532 nm), which is attributed to the ICT effect. Correspondingly, the fluorescence spectra of CC-CH were red-shifted from 563 nm to 626 nm with increasing solvent polarity (Figure 1b), suggesting that CC-CH is sensitive to polarity. To further explore the relationship between fluorescence emission and solvent polarity, we chose the solvent polarity parameter  $E_T(30)$  [50] for solute–solvent interactions at the microscopic level as a measure of the magnitude of solvent polarity. Typically, solvent polarity shows a positive correlation with  $E_T(30)$ . As shown in Figure 1c, the maximum emission wavelength of CC-CH in different polarity solvents had a good linear relationship with  $E_T(30)$  of the solvents after fitting calculations ( $y = 5.59x + 370.42$ ,  $R_r = 0.985$ ). Other than this, the molar extinction coefficients of CC-CH in different polarity solvents were all quite high (Table S1), and were all around  $80,000 \text{ M}^{-1}\text{cm}^{-1}$ . This shows excellent light absorption ability, which is undoubtedly beneficial for fluorescence imaging. The fluorescence quantum yields of CC-CH in different solvents were 12.2% (toluene), 12.5% (THF), 11.7% (EA), and 13.5% (DCM) (Table S1). In contrast, CC-CH showed weak fluorescence emission in DMSO with a fluorescence quantum yield of only 3.3%.

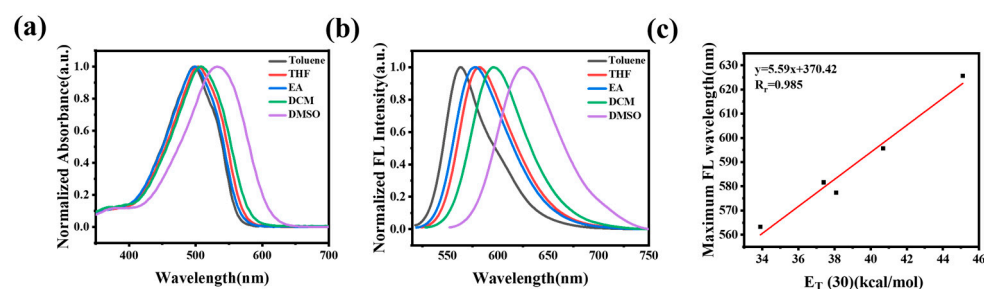


**Figure 1.** (a) Normalized absorption spectra of CC-CH in different polarity solvents. (b) Normalized fluorescence spectra of CC-CH in different polarity solvents. (c) Plot of the maximum emission wavelength of CC-CH in different polarity solvents vs.  $E_T(30)$ .

Similar to CC-CH, a positive solvatochromism of CC-Cl and a good linear relationship between the maximum emission wavelength of CC-Cl and  $E_T(30)$  of the solvents were also obtained (Figure 2). However, the maximum absorption and emission wavelengths of CC-Cl were both red-shifted by about 30 nm compared with CC-CH (Table S2), which is attributed to the introduction of the electron-withdrawing chlorine atom. In addition, CC-Cl had lower molar extinction coefficients and higher fluorescence quantum yields than CC-CH in different solvents (Table S2).

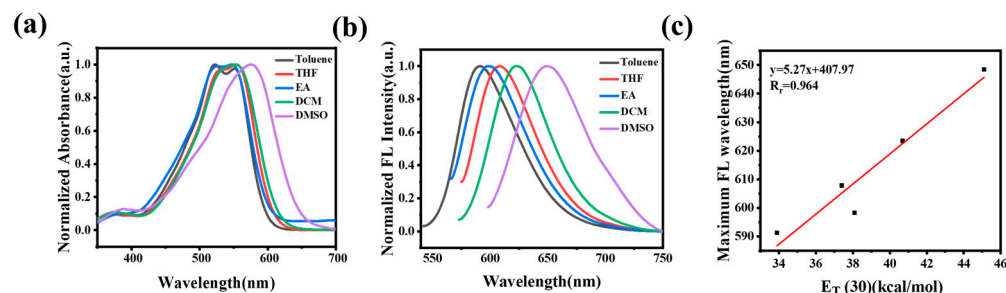


**Figure 2.** (a) Normalized absorption spectra of CC-Cl in different polarity solvents. (b) Normalized fluorescence spectra of CC-Cl in different polarity solvents. (c) Plot of the maximum emission wavelength of CC-Cl in different polarity solvents vs.  $E_T(30)$ .

In order to accurately evaluate the fluorescence intensity versus polarity, the fluorescence spectra of CC-CH and CC-Cl were measured in DMSO/toluene mixtures. As shown in Figure 3a, when increasing the proportion of toluene, the fluorescence spectra of CC-CH were blue-shifted and the corresponding fluorescence intensity was significantly enhanced. When the proportion of toluene was increased from 0% to 99%, the fluorescence intensity of CC-CH increased to about 76 times that of the original one. After nonlinear fitting calculations, there was a certain pattern between the fluorescence intensity of CC-CH and the toluene ratio, namely, the fluorescence intensity grew exponentially with increasing the toluene ratio (Figure 3c). The change in fluorescence emission of CC-Cl in DMSO/toluene mixtures was similar to CC-CH (Figure 3b), but the increase in fluorescence intensity was greater, becoming 103 times more than the original (Figure 3d). This suggests that CC-Cl may be more sensitive to the decrease in environmental polarity in comparison with CC-CH.

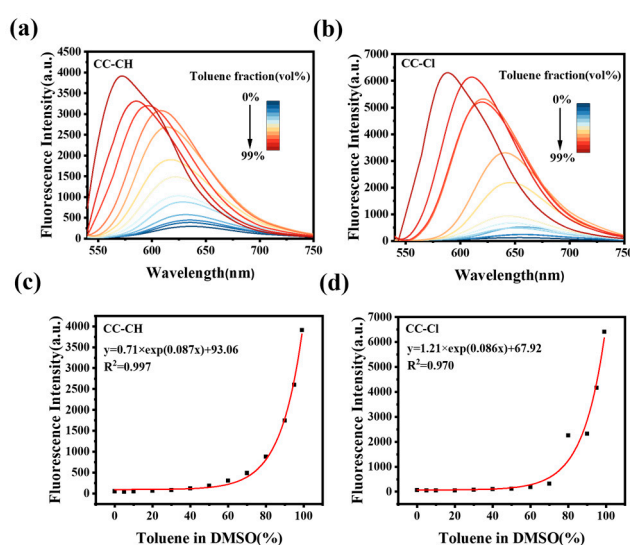


**Figure 3.** Fluorescence spectra of (a) CC-CH and (b) CC-Cl in DMSO/toluene mixtures with different toluene fractions. Plots of fluorescence intensity of (c) CC-CH and (d) CC-Cl in DMSO/toluene mixtures vs. different toluene fractions. CC-CH:  $\lambda_{ex} = 498$  nm, CC-Cl:  $\lambda_{ex} = 519$  nm.

Considering the diversity and complexity within cells, we also measured the fluorescence spectra of CC-CH and CC-Cl in H<sub>2</sub>O/1,4-dioxane mixtures (Figure S1a,b). Similar to the results in the DMSO/toluene mixtures, when the proportion of 1,4-dioxane was increased from 0% to 99%, the fluorescence intensities of CC-CH and CC-Cl rose by approximately 180 and 457 times, respectively (Figure S1c,d). The increase in fluorescence intensity of CC-Cl was also higher than CC-CH in the H<sub>2</sub>O/1,4-dioxane mixtures, further verifying that CC-Cl is more sensitive to low polarity environments than CC-CH. All of these results indicate that CC-CH and CC-Cl have polarity-sensitive properties and may be used as polarity-sensitive fluorescent probes.

## 2.2. LD-Specific Ability

At first, cytotoxicity assays were performed in three tumor cell lines (HepG-2, HeLa, and A549) and one normal cell line (HU-EVC) to assess the biocompatibility of CC-CH and CC-Cl as probes. The MTT results showed that the probes at 0–5  $\mu$ M concentrations had low cytotoxicity after 24 h of co-incubation with the four cell lines mentioned above, and the cell viability was greater than 80% (Figure S2). The cytotoxicity of CC-CH was slightly higher than CC-Cl, probably due to the introduction of the six membered ring, which increases the cytotoxicity of CC-CH.

In view of the diversity and complexity of the intracellular environment, anti-interference is particularly important for fluorescent probes. To comprehensively assess the effect of

the intracellular environment on CC-CH and CC-Cl, we tested a variety of potential interferences, including pH, anions and cations, hydrogen peroxide ( $H_2O_2$ ), and amino acids. As shown in Figure S3, the absorption spectra of CC-CH and CC-Cl showed little change in the pH 4–9 range, showing good pH stability. Moreover, the fluorescence intensity of CC-CH and CC-Cl changed less after the addition of various anions and cations,  $H_2O_2$ , and amino acids, indicating that CC-CH and CC-Cl have favorable anti-interference properties (Figure S4). The photostability testing of the probes and the commercial LD probe BODIPY 493/503 in HepG-2 cells showed that CC-CH and CC-Cl possessed more superior photostabilities than BODIPY 493/503 (Figure S5), and the fluorescence intensity remained more than 85% of the original fluorescence intensity after 10 min of continuous scanning with a confocal laser scanning microscope (CLSM). All of the above tests confirm that CC-CH and CC-Cl have various properties that fluorescent probes should have for cellular imaging.

To demonstrate that the probes could enter the cells and target the LDs, confocal fluorescence images of CC-CH and CC-Cl incubated with HepG-2 cells for different durations were firstly taken. CC-CH and CC-Cl already exhibited good fluorescence imaging after 1 h of co-incubation with HepG-2 cells at a low concentration (Figure S6). To further validate the specific targeting ability of CC-CH and CC-Cl to LDs, co-localization experiments with three commercial green-emitting organelle fluorescent probes were performed. As shown in Figure 4, CC-CH and CC-Cl achieved a high Pearson correlation coefficient ( $R_r$ ) of 0.97 with the commercial LD probe BODIPY 493/503, as well as overlapping almost completely at a three-dimensional level. However, CC-CH and CC-Cl specifically targeted LDs while overlapping poorly with the lysosomal probe Lyso Tracker Green (LTG) and the mitochondrial probe Mito Tracker Green (MTG) (Figures S7 and S8). The anti-light interference testing also indicated that the Pearson correlation coefficient with commercial LD probe BODIPY 493/503 had a high confidence (Figures S9 and S10). In addition to HepG-2 cells, co-localization experiments with BODIPY 493/503 were also performed in Hela cells and A549 cells (Figures S11 and S12), and the Pearson correlation coefficients were all above 0.95, indicating that CC-CH and CC-Cl have excellent LD targeting abilities in different cell lines.

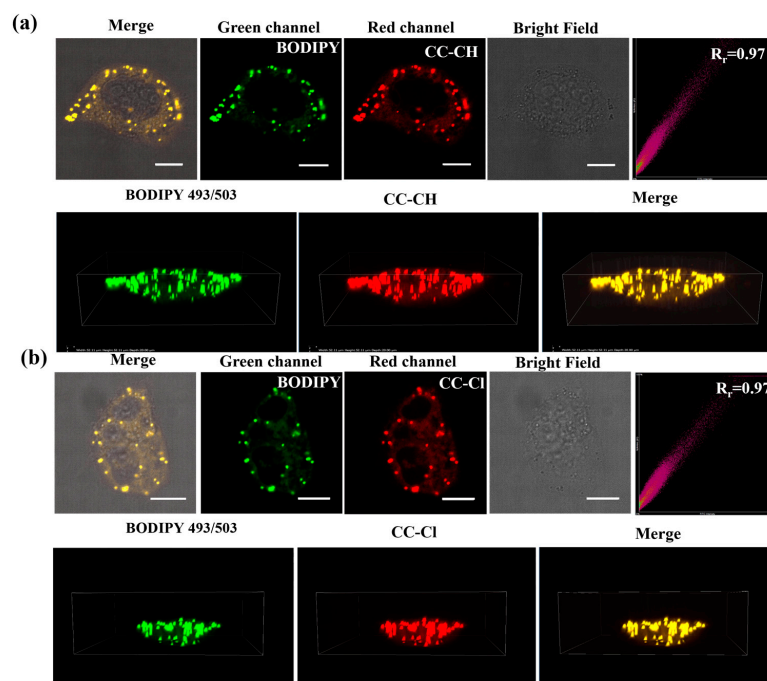


**Figure 4.** Colocalization images and three-dimensional images of (a) CC-CH (2.5  $\mu$ M) and (b) CC-Cl (2.5  $\mu$ M) with BODIPY 493/503 (0.2  $\mu$ M) in HepG-2 cells. Scale bar: 10  $\mu$ m. Green channel:  $\lambda_{ex}$  = 488 nm,  $\lambda_{em}$  = 500–530 nm. Red channel:  $\lambda_{ex}$  = 488 nm,  $\lambda_{em}$  = 568–643 nm.

### 2.3. Fluorescence Imaging of LDs Polarity Changes

To verify whether the probe could image changes in the polarity of intracellular LDs, HepG-2 cells were treated with oleic acid (OA) for 4 h, and then washed off and co-cubated with the probe. OA, a high nutrient that is extremely easily absorbed by cells, can decrease the polarity of intracellular LDs and promote the production of large amounts of endogenous LDs [51]. As shown in Figure 5a,c, the fluorescence in LDs markedly increased after treatment with OA compared to the untreated group, suggesting that the probe can be used to visualize changes in the polarity of intracellular LDs. Furthermore, there was a significant boost in the number and size of LDs after treatment with OA, suggesting that the probes can not only reveal changes in the polarity of intracellular LDs but also changes in the size and number of intracellular LDs. Quantitative analysis of the fold increase in the average intracellular fluorescence intensity revealed that the fluorescence increase of CC-Cl was more significant than CC-CH (Figure 5b,d). This result further demonstrates at the cellular imaging level that CC-Cl is more sensitive to a decrease in LD polarity compared with CC-CH.

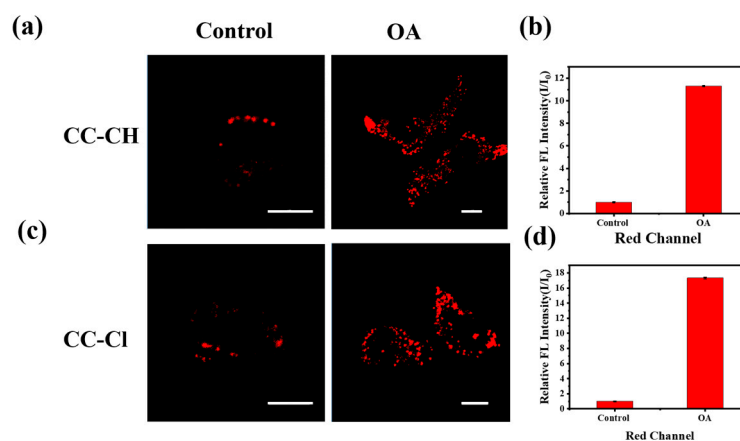


**Figure 5.** Confocal fluorescence images of HepG-2 cells treated with 0.1 mM OA for 4 h and then stained with (a) CC-CH and (c) CC-Cl. The relative fluorescence intensity ( $I/I_0$ ) of (b) CC-CH and (d) CC-Cl of the control and OA-treated groups in the red channel. Scale bar: 10  $\mu\text{m}$ . Red channel:  $\lambda_{\text{ex}} = 488 \text{ nm}$ ,  $\lambda_{\text{em}} = 568\text{--}643 \text{ nm}$ .

Methyl- $\beta$ -cyclodextrin (M- $\beta$ -CD), a recognized biomembrane cholesterol scavenger [52], is able to destroy the LD microenvironment, thereby increasing the polarity of LDs. To further verify the ability of the probe to indicate intracellular LD polarity changes, HepG-2 cells treated with M- $\beta$ -CD were stained with the probe (Figure S13). Compared with the control group, the fluorescence intensity of LDs in HepG-2 cells treated with M- $\beta$ -CD was somewhat attenuated, which successfully indicated the increase in the polarity in LDs. Both of these results demonstrate that CC-CH and CC-Cl can be used as indicators of the change in polarity of intracellular LDs.

### 2.4. Monitoring of LD Polarity Changes during Different Pathological Processes

As an important class of cellular injury models, inflammatory cells are crucial in medical research [53]. Lipopolysaccharide (LPS), as a major component of Gram-negative bacterial cell walls, is commonly used to obtain inflammatory cell models [54]. Therefore, we used LPS to induce an inflammatory cell model to explore the polarity changes of LDs in the inflammatory cell model. As shown in Figure 6, the fluorescence intensity gradually increased with the extension of LPS induction time, indicating that the polarity of LDs gradually decreases in the inflammatory cell model, which may be related to the accumulation of triglycerides within the LDs under the inflammatory state [55].

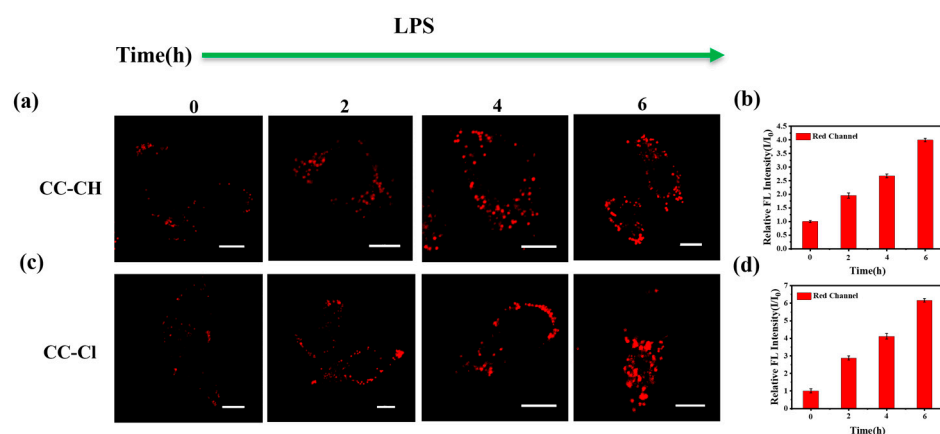


**Figure 6.** Confocal fluorescence images of HepG-2 cells treated with LPS for different times of 0, 2, 4, and 6 h and stained with (a) CC-CH and (c) CC-Cl. The relative fluorescence intensity ( $I/I_0$ ) of (b) CC-CH and (d) CC-Cl at different LPS treatment times. Scale bar: 10  $\mu\text{m}$ . Red channel:  $\lambda_{\text{ex}} = 488 \text{ nm}$ ,  $\lambda_{\text{em}} = 568\text{--}643 \text{ nm}$ .

Under starvation conditions, LDs release stored fatty acids (FAs) [56], which are available for mitochondrial catabolism to maintain normal cellular functions, and this process is accompanied by an increase in the polarity of LDs. To verify the phenomenon of increased polarity within LDs during this process, we used serum-free Earle's Balanced Salt Solution (EBSS) for nutrient deprivation of HepG-2 cells after the probes were pre-incubated. As shown in Figure 7, the fluorescence intensity gradually decreased with the prolongation of nutritional deprivation time, indicating a gradual increase in the polarity of LDs under starvation conditions.

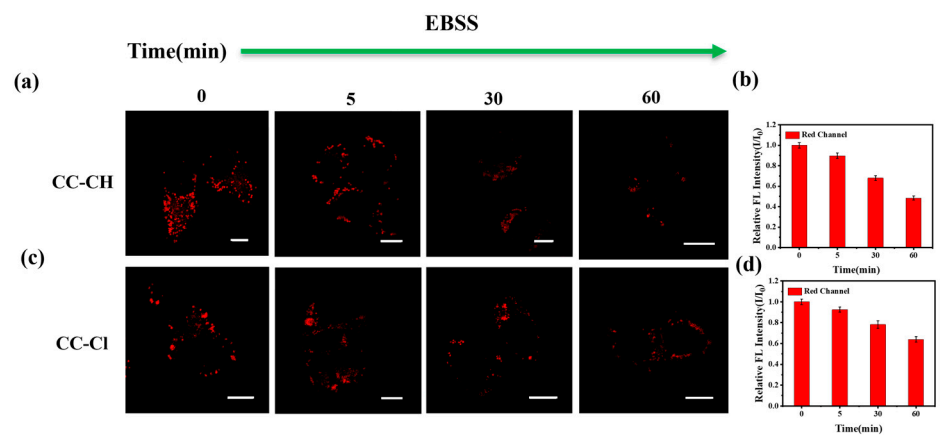


**Figure 7.** Confocal fluorescence images of HepG-2 cells stained with (a) CC-CH (2.5  $\mu\text{M}$ ) and (c) CC-Cl (2.5  $\mu\text{M}$ ) for 1 h and then incubated in EBSS for different times (0, 5, 30, 60 min). The relative fluorescence intensity ( $I/I_0$ ) of (b) CC-CH and (d) CC-Cl at different starvation times. Scale bar: 10  $\mu\text{m}$ . Red channel:  $\lambda_{\text{ex}} = 488 \text{ nm}$ ,  $\lambda_{\text{em}} = 568\text{--}643 \text{ nm}$ .

The oxidative stress state of cells has been shown to be closely related to numerous physiological and pathological processes [57]. It has been reported that high concentrations of  $\text{H}_2\text{O}_2$  can stimulate cells to enter a state of oxidative stress within a short period of time [58]. As shown in Figure 8, the fluorescence in the LDs gradually diminished with the extension of  $\text{H}_2\text{O}_2$  addition time, indicating an increase in the polarity in LDs, which may be due to lipid peroxidation in the oxidative stress state [59]. The above result indicates that CC-CH and CC-Cl are capable of monitoring  $\text{H}_2\text{O}_2$ -induced polarity changes in intracellular LDs under oxidative stress.

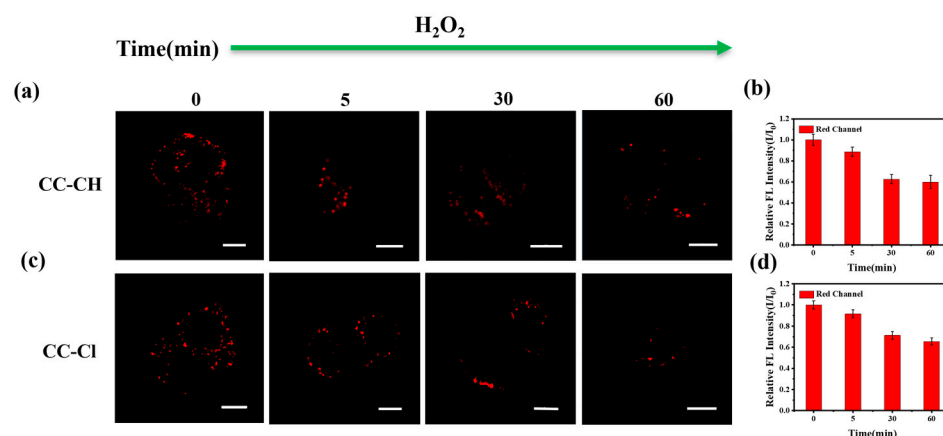


**Figure 8.** Confocal fluorescence images of HepG-2 cells stained with (a) CC-CH (2.5 μM) and (c) CC-Cl (2.5 μM) for 1 h and then incubated with 1 mM H<sub>2</sub>O<sub>2</sub> for different time (0, 5, 30, 60 min). The relative fluorescence intensity ( $I/I_0$ ) of (b) CC-CH and (d) CC-Cl at different H<sub>2</sub>O<sub>2</sub> stimulation times. Scale bar: 10 μm. Red channel:  $\lambda_{ex} = 488$  nm,  $\lambda_{em} = 568$ –643 nm.

### 3. Materials and Methods

#### 3.1. Materials and Instruments

All reagents were purchased from commercial sources (Innochem (Beijing, China), TCI (Shanghai, China), Sigma-Aldrich (Shanghai, China), Adamas-beta (Shanghai, China), Aladdin (Shanghai, China)) and used without further purification. All solvents and inorganic salts were purchased from Beijing Reagent, Sinopharm Chemical Reagent Beijing or General-Reagent, and used without further processing. Human cervical carcinoma cells (HeLa cells), human hepatocarcinoma cells (HepG-2 cells), human non-small cell lung cancer cell (A549 cells), and Human Umbilical Vein Endothelial Cells (HU-EVC cells) were purchased from the Center of Cells, Peking Union Medical College.

<sup>1</sup>H NMR and <sup>13</sup>C NMR spectra were obtained with Bruker Avance III 400 and Ascend 600 MHz spectrometers (Karlsruhe, Germany), respectively, using CDCl<sub>3</sub> or DMSO-d<sub>6</sub> as a solvent, and tetramethylsilane (TMS) was used as an internal standard. Electrospray Ionization Mass Spectrometry (ESI-MS) was conducted using a Thermo Fisher Scientific Q-Exactive spectrometer (Waltham, MA, USA). Absorption spectra were recorded on a Hitachi U-3900 ultraviolet–visible (UV-Vis) spectrophotometer (Tokyo, Japan). Fluorescence spectra were recorded on a Hitachi F-4600 spectrofluorometer (Tokyo, Japan). Absolute fluorescence quantum yields were measured in a Quantaaurus-QY absolute PL quantum yield spectrometer C11347 (Hamamatsu, Shizuoka, Japan).

#### 3.2. Synthesis and Characterization

The synthetic route to the CC-CH and CC-Cl probes is shown in Scheme S1. Their characterization (Figures S14–S18) and synthesis details of the intermediates [60] are provided in the Electronic Supplementary Information.

*7-(diethylamino)-3-((E)-((Z)-3-((E)-3-(7-(diethylamino)-2-oxo-2H-chromen-3-yl)-hydroxyallylidene)-2-oxocyclohexylidene) methyl)-2H-chromen-2-one* (CC-CH): Boron trioxide (1.05 g, 15 mmol) was added to a two-necked flask and then 8 mL anhydrous DMF was added under a nitrogen atmosphere. The temperature was raised to 120 °C and the mixture was stirred for 5 min. Then, 2-acetylcyclohexanone (133 mL, 1 mmol), tributyl borate (0.54 mL, 2 mmol), compound 2 (522 mg, 2.1 mmol), and 1, 2, 3, 4-tetrahydroquinoline (0.1 mL) were successively added, and the resulting mixture was stirred at 120 °C for 5 h. The mixture was extracted with dichloromethane (DCM) 3 times. The combined organic layers were washed with ultrapure water 6 times and dried over MgSO<sub>4</sub>. Finally, a red solid (CC-CH) (289 mg, 48%) was obtained by silica gel column purification. <sup>1</sup>H NMR (400 MHz, Chloroform-*d*)  $\delta$  17.03 (s, 1H), 7.77 (d,  $J = 15.2$  Hz, 1H), 7.71 (s, 2H), 7.60–7.50 (m, 2H), 7.34–7.28 (m, 2H), 6.61 (d,  $J = 9.0$  Hz, 2H), 6.50 (s, 2H), 3.49–3.39 (m, 8H), 2.70 (t,  $J = 6.1$  Hz, 4H), 1.81 (t,  $J = 6.2$  Hz, 2H), 1.29–1.18 (m, 12H). <sup>13</sup>C

NMR (151 MHz,  $\text{CDCl}_3$ -*d*)  $\delta$  186.54, 176.76, 161.83, 160.23, 156.40, 156.08, 151.71, 150.90, 145.47, 141.75, 137.37, 134.23, 129.97, 129.46, 126.66, 122.21, 116.90, 115.29, 109.51, 109.39, 109.14, 109.02, 108.63, 97.18, 96.83, 45.03, 44.92, 27.79, 24.23, 22.83, 12.50. HRMS (ESI-MS, *m/z*):  $[\text{M}+\text{H}]^+$  calcd for  $\text{C}_{36}\text{H}_{39}\text{N}_2\text{O}_6$ , 595.2803; Found, 595.2801.

*3,3'-(1E,3E,6E)-4-chloro-3-hydroxy-5-oxohepta-1,3,6-triene-1,7-diyl*)bis(7(diethylamino)-2H-chromen-2-one) (CC-Cl): Boron trioxide (1.05 g, 15 mmol) was added to a two-necked flask and then 8 mL anhydrous DMF was added under a nitrogen atmosphere. The temperature was raised to 120 °C and the mixture was stirred for 5 min. Then, 3-Chloroacetylacetone (118 mmL, 1 mmol), tributyl borate (0.54 mL, 2 mmol), compound 2 (522 mg, 2.1 mmol), and 1, 2, 3, 4-tetrahydroquinoline (0.1 mL) were successively added, and the resulting mixture was stirred at 120 °C for 5 h. The mixture was extracted with dichloromethane (DCM) 3 times. The combined organic layers were washed with ultrapure water 6 times and dried over  $\text{MgSO}_4$ . Finally, a red solid (CC-Cl) (332 mg, 56%) was obtained by silica gel column purification.  $^1\text{H}$  NMR (400 MHz,  $\text{CDCl}_3$ -*d*)  $\delta$  16.55 (s, 1H), 7.90 (d, *J* = 15.5 Hz, 2H), 7.79 (s, 2H), 7.64 (d, *J* = 15.5 Hz, 2H), 7.33 (d, *J* = 8.9 Hz, 2H), 6.61 (d, *J* = 9.0 Hz, 2H), 6.51 (s, 2H), 3.45 (q, *J* = 7.0 Hz, 8H), 1.26–1.22 (m, 12H).  $^{13}\text{C}$  NMR (Not obtained due to insufficient solubility). HRMS (ESI-MS, *m/z*):  $[\text{M}+\text{H}]^+$  calcd for  $\text{C}_{33}\text{H}_{34}\text{ClN}_2\text{O}_6$ , 589.2100; Found, 589.2101.

### 3.3. Photophysical Properties Measurements

CC-CH and CC-Cl were dissolved in DMSO to prepare a 1.0 mM stock solution. Afterwards, the stock solution was stored at  $-20$  °C for future use. The stock solution of CC-CH was diluted to 10  $\mu\text{M}$  with various solvents to measure the absorption and fluorescence spectra. The stock solution of CC-Cl was diluted to 20  $\mu\text{M}$  with various solvents to measure the absorption and fluorescence spectra. The excitation wavelength corresponded to the maximum absorption wavelength. The fluorescence spectra of CC-CH and CC-Cl were also measured in DMSO/toluene mixtures and  $\text{H}_2\text{O}/1,4$ -dioxane mixtures, respectively, to confirm the established relationship between the fluorescence of CC-CH and CC-Cl and the polarity of solvent mixtures. The fluorescence spectra of the DMSO/toluene system were measured using the maximum absorption wavelength of the probe in toluene as the excitation wavelength under identical conditions. Similarly, the fluorescence spectra of the  $\text{H}_2\text{O}/1,4$ -dioxane system were measured with the maximum absorption wavelength of the probe in 1,4-dioxane as the excitation wavelength.

The absorption spectra of CC-CH and CC-Cl in phosphate-buffered saline (PBS) with different pH values (pH 4–9, 1% DMSO) were measured to assess their pH stability. PBS with different pH values was calibrated with a pH meter before use.

The solutions of interfering substances for anti-interference testing were freshly prepared. Anti-interference testing was performed in PBS (pH = 7.4, 1% DMSO). The concentrations of all anions and cations,  $\text{H}_2\text{O}_2$ , and amino acids were 100  $\mu\text{M}$ .

### 3.4. Biological Evaluation

#### 3.4.1. Cell Cultures

The HepG-2, HeLa, and HU-EVC cells were cultured in a medium containing 89% Dulbecco's Modified Eagle Medium (DMEM), 10% FBS, 0.05%, 100  $\mu\text{g}/\text{mL}$  penicillin + 0.05%, and 100  $\mu\text{g}/\text{mL}$  streptomycin in a Petri dish under a 5%  $\text{CO}_2$  atmosphere at 37 °C for 24 h. The A549 cells were cultured in a medium containing 89% McCoy's 5A Medium (5A), 10% FBS, 0.05%, 100  $\mu\text{g}/\text{mL}$  penicillin + 0.05%, and 100  $\mu\text{g}/\text{mL}$  streptomycin in a Petri dish under a 5%  $\text{CO}_2$  atmosphere at 37 °C for 24 h.

#### 3.4.2. Cytotoxicity Assay of CC-CH and CC-Cl

The probes cytotoxicity to HeLa, HepG-2, A549, and HU-EVC cells was evaluated by an MTT (3-(4,5-dimethylthiazol-2-yl)-2,5-diphenyltetrazolium bromide) assay. Exponentially grown cells were seeded at a density of  $5 \times 10^4$  cells/mL into 96-well plates and cultured for 24 h. Then, the cells were treated with tested samples at different concentrations (1, 2, 3, 4, and 5  $\mu\text{M}$ ) for 24 h. Control cells were treated with cell culture broth alone.

After incubation at 37 °C for 24 h, the MTT assay was conducted. The absorbance was measured at 570 nm using a multifunctional microplate reader. The relative cell viability (%) was calculated by the following formula:

$$\text{cell viability (\%)} = \text{OD}_{\text{treated}} / \text{OD}_{\text{control}} \times 100.$$

#### 3.4.3. Cell Imaging at Different Incubation Times and Photostability Testing

HepG-2 cells were incubated with CC-CH (2.5  $\mu\text{M}$ ) or CC-Cl (2.5  $\mu\text{M}$ ) for different incubation durations (0.5 h, 1 h, 2 h), washed thrice with PBS, and then placed in 1 mL PBS for imaging with CLSM. Fluorescence signals were collected at 568–643 nm using a laser at 488 nm as the excitation source.

HepG-2 cells were incubated with CC-CH/CC-Cl (2.5  $\mu\text{M}$ ) and BODIPY 493/503 (0.2  $\mu\text{M}$ ) and then irradiated with CLSM for 10 min continuously (scan every two seconds, 300 times in total). The change in fluorescence intensity was recorded. The fluorescence signals were collected at 568–643 nm for CC-CH/CC-Cl and 500–530 nm for BODIPY 493/503 using a laser at 488 nm as the excitation source.

#### 3.4.4. Cellular Co-Localization Experiments

HepG-2, HeLa, and A549 cells were incubated with CC-CH (2.5  $\mu\text{M}$ ) or CC-Cl (2.5  $\mu\text{M}$ ) for 1 h, washed thrice with PBS, and then incubated with BODIPY 493/503 (0.2  $\mu\text{M}$ ), LTG (0.2  $\mu\text{M}$ ), or MTG (0.2  $\mu\text{M}$ ) for 10 min. Confocal fluorescence images were captured with the green channel ( $\lambda_{\text{ex}} = 488 \text{ nm}$ ,  $\lambda_{\text{em}} = 500\text{--}530 \text{ nm}$ ) for the organelle-targeted fluorescent probe and the red channel ( $\lambda_{\text{ex}} = 488 \text{ nm}$ ,  $\lambda_{\text{em}} = 568\text{--}643 \text{ nm}$ ) for CC-CH and CC-Cl.

#### 3.4.5. Visualization of LD Polarity Changes in HepG-2 Cells

HepG-2 cells were treated with 0.1 mM OA for 4 h and washed thrice with PBS, then the cells were incubated with CC-CH (2.5  $\mu\text{M}$ ) or CC-Cl (2.5  $\mu\text{M}$ ) for 1 h. In the control group, HepG-2 cells were only incubated with CC-CH (2.5  $\mu\text{M}$ ) or CC-Cl (2.5  $\mu\text{M}$ ) for 1 h. Fluorescence images were collected with CLSM. Red channel:  $\lambda_{\text{ex}} = 488 \text{ nm}$ ,  $\lambda_{\text{em}} = 568\text{--}643 \text{ nm}$ .

HepG-2 cells were treated with 2 mg/mL M- $\beta$ -CD for 2 h, washed thrice with PBS, and then incubated with CC-CH (2.5  $\mu\text{M}$ ) or CC-Cl (2.5  $\mu\text{M}$ ) for 1 h. In the control group, HepG-2 cells were only incubated with CC-CH (2.5  $\mu\text{M}$ ) or CC-Cl (2.5  $\mu\text{M}$ ) for 1 h. The fluorescence images were collected with CLSM. Red channel:  $\lambda_{\text{ex}} = 488 \text{ nm}$ ,  $\lambda_{\text{em}} = 568\text{--}643 \text{ nm}$ .

HepG-2 cells were treated with LPS for different durations of 0, 2, 4, and 6 h and then the cells were incubated with CC-CH (2.5  $\mu\text{M}$ ) or CC-Cl (2.5  $\mu\text{M}$ ) for 1 h. Fluorescence images were collected with CLSM. Red channel:  $\lambda_{\text{ex}} = 488 \text{ nm}$ ,  $\lambda_{\text{em}} = 568\text{--}643 \text{ nm}$ .

HepG-2 cells were incubated with CC-CH (2.5  $\mu\text{M}$ ) or CC-Cl (2.5  $\mu\text{M}$ ) for 1 h, washed thrice with PBS, and then treated with 1 mL EBSS or 1 mM  $\text{H}_2\text{O}_2$  for different durations (0, 5, 30, or 60 min). Fluorescence images were collected with CLSM. Red channel:  $\lambda_{\text{ex}} = 488 \text{ nm}$ ,  $\lambda_{\text{em}} = 568\text{--}643 \text{ nm}$ .

## 4. Conclusions

In summary, we have constructed two fluorescent probes with the D–A–D structure, CC-CH and CC-Cl, which are sensitive to polarity and exhibit positive solvatochromism due to the ICT property. Cell experiments showed that CC-CH and CC-Cl show low cytotoxicity, good photostability, and specific targeting of LDs. The excellent properties of the two probes in solution and in living cells enable them to be used for monitoring LD polarity changes in different pathological processes, including inflammatory responses, nutrient deprivation, and oxidative stress. CC-CH and CC-Cl present as potential tools for probing changes in LD polarity.

**Supplementary Materials:** The following supporting information can be downloaded at: <https://www.mdpi.com/article/10.3390/molecules28186626/s1>, Table S1: Photophysical properties of CC-CH in different polarity solvents; Table S2: Photophysical properties of CC-Cl in different

polarity solvents; Figure S1: Fluorescence changes in CC-CH and CC-Cl in H<sub>2</sub>O/1,4-dioxane mixtures with different 1,4-dioxane fractions; Figure S2: Cytotoxicity testing; Figure S3: pH stability testing; Figure S4: Anti-interference testing; Figure S5: Photostability testing in HepG-2 cells; Figure S6: CLSM images of CC-CH and CC-Cl in HepG-2 cells at different incubation times; Figure S7: Colocalization images of CC-CH with LTG and MTG in HepG-2 cells; Figure S8: Colocalization images of CC-Cl with LTG and MTG in HepG-2 cells; Figure S9: Anti-light interference testing of CC-CH and BODIPY 493/503; Figure S10: Anti-light interference testing of CC-Cl and BODIPY 493/503; Figure S11: Colocalization images of CC-CH with BODIPY 493/503 in different cell lines; Figure S12: Colocalization images of CC-Cl with BODIPY 493/503 in different cell lines; Figure S13: Visualization of the M- $\beta$ -CD-induced LD polarity increase in living cells; Figures S14–S18: NMR and MS spectra; Scheme S1: Synthetic route to CC-CH and CC-Cl; Synthesis details of the intermediates.

**Author Contributions:** L.S.: methodology, software, data curation, writing—original draft, visualization. X.L.: formal analysis, methodology. X.Z.: formal analysis, project administration. J.W.: formal analysis, visualization. H.R.: visualization, methodology. W.L.: conceptualization, writing—review and editing, supervision, project administration. P.W.: supervision, funding acquisition. All authors have read and agreed to the published version of the manuscript.

**Funding:** This work was supported by the National Key Research and Development Program of China (No. 2022YFA1207600) and the National Natural Science Foundation of China (Grant No. 62375272).

**Institutional Review Board Statement:** Not applicable.

**Informed Consent Statement:** Not applicable.

**Data Availability Statement:** The data from this study are available from the corresponding author upon reasonable request.

**Conflicts of Interest:** The authors declare no conflict of interest.

**Sample Availability:** Samples of the compounds CC-CH and CC-Cl are available from the authors.

## References

1. Olzmann, J.A.; Carvalho, P. Dynamics and functions of lipid droplets. *Nat. Rev. Mol. Cell Biol.* **2018**, *20*, 137–155. [[CrossRef](#)] [[PubMed](#)]
2. Thiam, A.R.; Farese, R.V., Jr.; Walther, T.C. The biophysics and cell biology of lipid droplets. *Nat. Rev. Mol. Cell Biol.* **2013**, *14*, 775–786. [[CrossRef](#)] [[PubMed](#)]
3. Zadoorian, A.; Du, X.; Yang, H. Lipid droplet biogenesis and functions in health and disease. *Nat. Rev. Endocrinol.* **2023**, *19*, 443–459. [[CrossRef](#)] [[PubMed](#)]
4. Thiam, A.R.; Ikonen, E. Lipid Droplet Nucleation. *Trends Cell Biol.* **2021**, *31*, 108–118. [[CrossRef](#)] [[PubMed](#)]
5. Walther, T.C.; Chung, J.; Farese, R.V., Jr. Lipid Droplet Biogenesis. *Annu. Rev. Cell Dev. Biol.* **2017**, *33*, 491–510. [[CrossRef](#)]
6. Bersuker, K.; Olzmann, J.A. Establishing the lipid droplet proteome: Mechanisms of lipid droplet protein targeting and degradation. *Biochim. Biophys. Acta* **2017**, *1862*, 1166–1177. [[CrossRef](#)] [[PubMed](#)]
7. Kory, N.; Farese, R.V., Jr.; Walther, T.C. Targeting Fat: Mechanisms of Protein Localization to Lipid Droplets. *Trends Cell Biol.* **2016**, *26*, 535–546. [[CrossRef](#)]
8. Barbosa, A.D.; Sinioglou, S. Function of lipid droplet-organelle interactions in lipid homeostasis. *Biochim. Biophys. Acta* **2017**, *1864*, 1459–1468. [[CrossRef](#)]
9. Geltinger, F.; Schartel, L.; Wiederstein, M.; Tevini, J.; Aigner, E.; Felder, T.K.; Rinnerthaler, M. Friend or Foe: Lipid Droplets as Organelles for Protein and Lipid Storage in Cellular Stress Response, Aging and Disease. *Molecules* **2020**, *25*, 5053. [[CrossRef](#)]
10. Herker, E.; Vieyres, G.; Beller, M.; Krahmer, N.; Bohnert, M. Lipid Droplet Contact Sites in Health and Disease. *Trends Cell Biol.* **2021**, *31*, 345–358. [[CrossRef](#)]
11. Henne, W.M. The (social) lives, deaths, and biophysical phases of lipid droplets. *Curr. Opin. Cell Biol.* **2023**, *82*, 102178. [[CrossRef](#)] [[PubMed](#)]
12. Seibert, J.T.; Najt, C.P.; Heden, T.D.; Mashek, D.G.; Chow, L.S. Muscle Lipid Droplets: Cellular Signaling to Exercise Physiology and Beyond. *Trends Endocrinol. Metab.* **2020**, *31*, 928–938. [[CrossRef](#)] [[PubMed](#)]
13. Chitraju, C.; Mejhert, N.; Haas, J.T.; Diaz-Ramirez, L.G.; Grueter, C.A.; Imbriglio, J.E.; Pinto, S.; Koliwad, S.K.; Walther, T.C.; Farese, R.V., Jr. Triglyceride Synthesis by DGAT1 Protects Adipocytes from Lipid-Induced ER Stress during Lipolysis. *Cell Metab.* **2017**, *26*, 407–418. [[CrossRef](#)] [[PubMed](#)]
14. Piccolis, M.; Bond, L.M.; Kampmann, M.; Pulimeno, P.; Chitraju, C.; Jayson, C.B.K.; Vaites, L.P.; Boland, S.; Lai, Z.W.; Gabriel, K.R.; et al. Probing the Global Cellular Responses to Lipotoxicity Caused by Saturated Fatty Acids. *Mol. Cell* **2019**, *74*, 32–44. [[CrossRef](#)] [[PubMed](#)]

15. Garcia, E.J.; Liao, P.-C.; Tan, G.; Vevea, J.D.; Sing, C.N.; Tsang, C.A.; McCaffery, J.M.; Boldogh, I.R.; Pon, L.A. Membrane dynamics and protein targets of lipid droplet microautophagy during ER stress-induced proteostasis in the budding yeast, *Saccharomyces cerevisiae*. *Autophagy* **2020**, *17*, 2363–2383. [[CrossRef](#)]
16. Henne, W.M.; Reese, M.L.; Goodman, J.M. The assembly of lipid droplets and their roles in challenged cells. *EMBO J.* **2018**, *37*, e98947. [[CrossRef](#)]
17. Welte, M.A.; Gould, A.P. Lipid droplet functions beyond energy storage. *Biochim. Biophys. Acta* **2017**, *1862*, 1260–1272. [[CrossRef](#)]
18. Pereira-Dutra, F.S.; Bozza, P.T. Lipid droplets diversity and functions in inflammation and immune response. *Expert Rev. Proteom.* **2021**, *18*, 809–825. [[CrossRef](#)]
19. Pereira-Dutra, F.S.; Teixeira, L.; de Souza Costa, M.F.; Bozza, P.T. Fat, fight, and beyond: The multiple roles of lipid droplets in infections and inflammation. *J. Leukoc. Biol.* **2019**, *106*, 563–580. [[CrossRef](#)]
20. Getiye, Y.; Rice, T.A.; Phillips, B.D.; Carrillo, D.F.; He, G. Dysregulated lipolysis and lipophagy in lipid droplets of macrophages from high fat diet-fed obese mice. *J. Cell. Mol. Med.* **2022**, *26*, 4825–4836. [[CrossRef](#)]
21. Park, C.Y.; Kim, D.; Seo, M.K.; Kim, J.; Choe, H.; Kim, J.-H.; Hong, J.P.; Lee, Y.J.; Heo, Y.; Kim, H.J.; et al. Dysregulation of Lipid Droplet Protein Expression in Adipose Tissues and Association with Metabolic Risk Factors in Adult Females with Obesity and Type 2 Diabetes. *J. Nutr.* **2023**, *153*, 691–702. [[CrossRef](#)]
22. Goldberg, I.J.; Reue, K.; Abumrad, N.A.; Bickel, P.E.; Cohen, S.; Fisher, E.A.; Galis, Z.S.; Granneman, J.G.; Lewandowski, E.D.; Murphy, R.; et al. Deciphering the Role of Lipid Droplets in Cardiovascular Disease. *Circulation* **2018**, *138*, 305–315. [[CrossRef](#)] [[PubMed](#)]
23. Zhang, B.; Li, X.; Liu, G.; Zhang, C.; Zhang, X.; Shen, Q.; Sun, G.; Sun, X. Peroxiredoxin-4 ameliorates lipotoxicity-induced oxidative stress and apoptosis in diabetic cardiomyopathy. *Biomed. Pharmacother.* **2021**, *141*, 111780. [[CrossRef](#)]
24. Gluchowski, N.L.; Becuwe, M.; Walther, T.C.; Farese, R.V., Jr. Lipid droplets and liver disease: From basic biology to clinical implications. *Nat. Rev. Gastroenterol. Hepatol.* **2017**, *14*, 343–355. [[CrossRef](#)] [[PubMed](#)]
25. Scorletti, E.; Carr, R.M. A new perspective on NAFLD: Focusing on lipid droplets. *J. Hepatol.* **2022**, *76*, 934–945. [[CrossRef](#)] [[PubMed](#)]
26. Shih, L.-M.; Tang, H.-Y.; Lynn, K.-S.; Huang, C.-Y.; Ho, H.-Y.; Cheng, M.-L. Stable Isotope-Labeled Lipidomics to Unravel the Heterogeneous Development Lipotoxicity. *Molecules* **2018**, *23*, 2862. [[CrossRef](#)] [[PubMed](#)]
27. Imai, Y.; Cousins, R.S.; Liu, S.; Phelps, B.M.; Promes, J.A. Connecting pancreatic islet lipid metabolism with insulin secretion and the development of type 2 diabetes. *Ann. N. Y. Acad. Sci.* **2019**, *1461*, 53–72. [[CrossRef](#)]
28. Tong, X.; Dai, C.; Walker, J.T.; Nair, G.G.; Kennedy, A.; Carr, R.M.; Hebrok, M.; Powers, A.C.; Stein, R. Lipid Droplet Accumulation in Human Pancreatic Islets Is Dependent On Both Donor Age and Health. *Diabetes* **2020**, *69*, 342–354. [[CrossRef](#)]
29. Tong, X.; Liu, S.; Stein, R.; Imai, Y. Lipid Droplets' Role in the Regulation of  $\beta$ -Cell Function and  $\beta$ -Cell Demise in Type 2 Diabetes. *Endocrinology* **2022**, *163*, bqac007. [[CrossRef](#)]
30. Farmer, B.C.; Walsh, A.E.; Kluemper, J.C.; Johnson, L.A. Lipid Droplets in Neurodegenerative Disorders. *Front. Neurosci.* **2020**, *14*, 742. [[CrossRef](#)]
31. Yamazaki, Y.; Zhao, N.; Caulfield, T.R.; Liu, C.-C.; Bu, G. Apolipoprotein E and Alzheimer disease: Pathobiology and targeting strategies. *Nat. Rev. Neurosci.* **2019**, *15*, 501–518. [[CrossRef](#)] [[PubMed](#)]
32. Petan, T.; Jarc, E.; Jusović, M. Lipid Droplets in Cancer: Guardians of Fat in a Stressful World. *Molecules* **2018**, *23*, 1941. [[CrossRef](#)] [[PubMed](#)]
33. Schwartzburd, P. Lipid droplets: Could they be involved in cancer growth and cancer–microenvironment communications? *Cancer Commun.* **2022**, *42*, 83–87. [[CrossRef](#)] [[PubMed](#)]
34. Hu, J.; Sun, Y.; Geng, X.; Wang, J.; Guo, Y.; Qu, L.; Zhang, K.; Li, Z. High-fidelity carbon dots polarity probes: Revealing the heterogeneity of lipids in oncology. *Light Sci. Appl.* **2022**, *11*, 185. [[CrossRef](#)] [[PubMed](#)]
35. Pu, Y.; Huang, R.; Chai, L.; Yang, H.; Wang, D.; Wei, Z.; Zhan, Z. Multimode evaluating the fluctuation of lipid droplets polarity in acute kidney injury and tumor models. *Sensor. Actuat. B Chem.* **2023**, *380*, 133343. [[CrossRef](#)]
36. Liu, Y.; Li, Y.; Koo, S.; Sun, Y.; Liu, Y.; Liu, X.; Pan, Y.; Zhang, Z.; Du, M.; Lu, S.; et al. Versatile Types of Inorganic/Organic NIR-IIa/IIb Fluorophores: From Strategic Design toward Molecular Imaging and Theranostics. *Chem. Rev.* **2021**, *122*, 209–268. [[CrossRef](#)]
37. Vahrmeijer, A.L.; Hutteman, M.; van der Vorst, J.R.; van de Velde, C.J.H.; Frangioni, J.V. Image-guided cancer surgery using near-infrared fluorescence. *Nat. Rev. Clin. Oncol.* **2013**, *10*, 507–518. [[CrossRef](#)]
38. Fam, T.K.; Klymchenko, A.S.; Collot, M. Recent Advances in Fluorescent Probes for Lipid Droplets. *Materials* **2018**, *11*, 1768. [[CrossRef](#)]
39. Tian, H., Jr.; Sedgwick, A.C.; Han, H.-H.; Sen, S.; Chen, G.-R.; Zang, Y.; Sessler, J.L.; James, T.D.; Li, J.; He, X.-P. Fluorescent probes for the imaging of lipid droplets in live cells. *Coord. Chem. Rev.* **2021**, *427*, 213577. [[CrossRef](#)]
40. Zhao, Y.; Shi, W.; Li, X.; Ma, H. Recent advances in fluorescent probes for lipid droplets. *Chem. Commun.* **2022**, *58*, 1495–1509. [[CrossRef](#)]
41. Xiao, H.; Li, P.; Tang, B. Recent progresses in fluorescent probes for detection of polarity. *Coord. Chem. Rev.* **2021**, *427*, 213582. [[CrossRef](#)]
42. Sasaki, S.; Drummen, G.P.C.; Konishi, G.-I. Recent advances in twisted intramolecular charge transfer (TICT) fluorescence and related phenomena in materials chemistry. *J. Mater. Chem. C* **2016**, *4*, 2731–2743. [[CrossRef](#)]

43. Wang, C.; Chi, W.; Qiao, Q.; Tan, D.; Xu, Z.; Liu, X. Twisted intramolecular charge transfer (TICT) and twists beyond TICT: From mechanisms to rational designs of bright and sensitive fluorophores. *Chem. Soc. Rev.* **2021**, *50*, 12656–12678. [[CrossRef](#)] [[PubMed](#)]
44. Yin, J.; Peng, M.; Ma, Y.; Guo, R.; Lin, W. Rational design of a lipid-droplet-polarity based fluorescent probe for potential cancer diagnosis. *Chem. Commun.* **2018**, *54*, 12093–12096. [[CrossRef](#)]
45. Collot, M.; Bou, S.; Fam, T.K.; Richert, L.; Mély, Y.; Danglot, L.; Klymchenko, A.S. Probing Polarity and Heterogeneity of Lipid Droplets in Live Cells Using a Push–Pull Fluorophore. *Anal. Chem.* **2019**, *91*, 1928–1935. [[CrossRef](#)]
46. Lin, B.; Li, Z.; Zan, Q.; Fan, L.; Shu, Y.; Wang, J. A fluorescent probe for lipid droplet polarity imaging with low viscosity crosstalk. *Analyst* **2023**, *148*, 3285–3294. [[CrossRef](#)]
47. Pei, S.; Li, H.; Li, J.; Liu, Y.; Zhang, G.; Shi, L.; Liang, W.; Zhang, C.; Shuang, S.; Dong, C. Synthesis of a Red-Emitting Polarity-Sensitive Fluorescent Probe Based on ICT and Visualization for Lipid Droplet Dynamic Processes. *ACS Biomater. Sci. Eng.* **2023**, *9*, 3590–3596. [[CrossRef](#)]
48. Peng, G.; Dai, J.; Zhou, R.; Liu, G.; Liu, X.; Yan, X.; Liu, F.; Sun, P.; Wang, C.; Lu, G. Highly Efficient Red/NIR-Emissive Fluorescent Probe with Polarity-Sensitive Character for Visualizing Cellular Lipid Droplets and Determining Their Polarity. *Anal. Chem.* **2022**, *94*, 12095–12102. [[CrossRef](#)]
49. Li, X.; Liu, W.; Zheng, X.; Jiang, M.; Guo, Y.; Sha, J.; Wu, J.; Ren, H.; Gao, H.; Wang, S.; et al. Lipid droplet targeting-guided hypoxic photodynamic therapy with curcumin analogs. *Chem. Commun.* **2023**, *59*, 4181–4184. [[CrossRef](#)]
50. Reichardt, C. Solvatochromic Dyes as Solvent Polarity Indicators. *Chem. Rev.* **1994**, *94*, 2319–2358. [[CrossRef](#)]
51. Zhou, X.; Mo, Z.; Li, Y.; Huang, L.; Yu, S.; Ge, L.; Hu, Y.; Shi, S.; Zhang, L.; Wang, L.; et al. Oleic acid reduces steroidogenesis by changing the lipid type stored in lipid droplets of ovarian granulosa cells. *J. Anim. Sci. Biotechnol.* **2022**, *13*, 27. [[CrossRef](#)] [[PubMed](#)]
52. Abe, M.; Kobayashi, T. Imaging cholesterol depletion at the plasma membrane by methyl- $\beta$ -cyclodextrin. *J. Lipid Res.* **2021**, *62*, 100077. [[CrossRef](#)] [[PubMed](#)]
53. Geyer, C.E.; Mes, L.; Newling, M.; den Dunnen, J.; Hoepel, W. Physiological and Pathological Inflammation Induced by Antibodies and Pentraxins. *Cells* **2021**, *10*, 1175. [[CrossRef](#)] [[PubMed](#)]
54. McQuade, R.M.; Bandara, M.; Diwakarla, S.; Sahakian, L.; Han, M.N.; Al Thaalibi, M.; Di Natale, M.R.; Tan, M.; Harwood, K.H.; Schneider-Futschik, E.K.; et al. Gastrointestinal consequences of lipopolysaccharide-induced lung inflammation. *Inflamm. Res.* **2022**, *72*, 57–74. [[CrossRef](#)]
55. Dierendonck, X.A.M.H.; Vrieling, F.; Smeehuijzen, L.; Deng, L.; Boogaard, J.P.; Croes, C.-A.; Temmerman, L.; Wetzels, S.; Biessen, E.; Kersten, S.; et al. Triglyceride breakdown from lipid droplets regulates the inflammatory response in macrophages. *Proc. Natl. Acad. Sci. USA* **2022**, *119*, e2114739119. [[CrossRef](#)]
56. Rambold, A.S.; Cohen, S.; Lippincott-Schwartz, J. Fatty Acid Trafficking in Starved Cells: Regulation by Lipid Droplet Lipolysis, Autophagy, and Mitochondrial Fusion Dynamics. *Dev. Cell* **2015**, *32*, 678–692. [[CrossRef](#)]
57. Szewczyk-Golec, K.; Czuczejko, J.; Tylzanowski, P.; Lecka, J. Strategies for Modulating Oxidative Stress under Diverse Physiological and Pathological Conditions. *Oxid. Med. Cell. Longev.* **2018**, *2018*, 3987941. [[CrossRef](#)]
58. Ransy, C.; Vaz, C.; Lombès, A.; Bouillaud, F. Use of H<sub>2</sub>O<sub>2</sub> to Cause Oxidative Stress, the Catalase Issue. *Int. J. Mol. Sci.* **2020**, *21*, 10.3390/molecules281866269149. [[CrossRef](#)]
59. Yin, H.; Xu, L.; Porter, N.A. Free Radical Lipid Peroxidation: Mechanisms and Analysis. *Chem. Rev.* **2011**, *111*, 5944–5972. [[CrossRef](#)]
60. Zhang, Y.; Teng, H.; Gao, Y.; Afzal, M.W.; Tian, J.; Chen, X.; Tang, H.; James, T.D.; Guo, Y. A general strategy for selective detection of hypochlorous acid based on triazolopyridine formation. *Chin. Chem. Lett.* **2020**, *31*, 2917–2920. [[CrossRef](#)]

**Disclaimer/Publisher’s Note:** The statements, opinions and data contained in all publications are solely those of the individual author(s) and contributor(s) and not of MDPI and/or the editor(s). MDPI and/or the editor(s) disclaim responsibility for any injury to people or property resulting from any ideas, methods, instructions or products referred to in the content.